

Title: Inflight Fluidic Fibre Printing Towards Array and 3D Optoelectronic and Sensing

Architectures

Authors: Wenyu Wang^{1,2}, Karim Ouaras^{1,2}, Alexandra L. Rutz¹, Xia Li^{1,2}, Magda Gerigk^{1,2}, Tobias E. Naegele¹, George G. Malliaras¹, Yan Yan Shery Huang^{1,2*}

Affiliations

¹ Department of Engineering, University of Cambridge, Cambridge CB2 1PZ, UK

² The Nanoscience Centre, University of Cambridge, Cambridge CB3 0FF, UK

*corresponding author: yysh2@cam.ac.uk

Abstract: Scalability and device-integration have been prevailing issues limiting our ability in harnessing the full potential of small-diameter conducting fibres. We report inflight fluidic fibre printing, a rapid, low-cost route that integrates the entire process of conducting fibre production and fibre-to-circuit connection, in a single step under sub-100 °C ambient atmospheres. Metallic (silver) or organic (PEDOT:PSS) fibres with 1-3 µm diameter are fabricated, and the fibre arrays exhibit over 95 % transmittance in the 350-750 nm region. We exploit combinations of the unique fibre characteristics: directionality, high surface-area-to-volume ratio, and permissiveness, along with transparency and conductivity. Using PEDOT:PSS fibres as a cell-interfaced impedimetric sensor and a moisture sensor, we show that even a single fibre component can achieve complex functions or outperform conventional film-based devices. The capability to design suspended fibres and networks of homo-, hetero- cross-junctions, paves the way to applications including flow-permissive devices, and 3D optoelectronic and sensor architectures.

MAIN TEXT

Introduction

Small-diameter conducting fibres possess unique morphological, mechanical and optical properties such as high aspect-ratio, low bending stiffness, directionality and transparency that set them apart from other classes of conducting, film-based micro-nano-structures (1–3). Orderly assembling thin conducting fibres into an array or three-dimensional (3D) structures up-scales their functional performance for device coupling. Developing new strategies to control rapid synthesis, patterning and integration of these conducting elements into a device architecture could mark an important step in enabling new device functions and electronic designs (4, 5). To-date, conducting micro/nano-scaled fibres have been produced and assembled in a number of ways, from transferring of chemically-grown nanofibers/wires (6, 7), writing electrohydrodynamically-deposited lines (8, 9), to drawing ultra-long fibres (10, 11), wet-spinning of fibres (12–14) and 2D/3D direct printing (15–18). These novel conducting structures have enabled a number of applications, including transparent and flexible electrodes (19–22), conducting yarns (23), tissue engineering scaffolds (24), and bioelectronics applications (25).

Despite these developments, existing fabrication techniques do not readily allow the assembly of fibre architectures leading to device functions that exploit combinations of the unique fibre characteristics: directionality, high surface-area-to-volume ratio, and permissiveness, along with transparency and conductivity. With their small diameter (micro/nano-scaled) and high aspect ratio (>100), manipulation of thin fibres at the single fibre level could be remarkably intricate and slow. Bonding and connecting the fibres with minimised contact resistance presents a major challenge for circuitry creation. As a result, most existing applications of fibre-based transparent conductors are substrate-based (17, 26). The underlying substrates can dominate the opto-mechanical properties of the transparent conductor in the final device setting; further, the permissive, high surface area-to-volume ratio qualities of a fibre array are completely lost. In

addition, from fibre-synthesis to device integration, a multi-step procedure, or post-synthesis fibre treatment are often required to obtain adequate on-circuit, fibre bond-to-bond conductivity (10, 27). This in turn restricts the materials library of conductive fibres that can be used.

Here, we develop inflight fluidic fibre printing (iFFP): a one-step process working at sub-100°C, which creates and *in-situ* bonds thin conducting fibre array, either suspended or on a surface, without needing any post-processing. By optimizing the fibre sizing, we show iFFP as a versatile technique for rapid on-circuit creation of small diameter (~1-3 µm thick) transparent conducting fibres of vastly dissimilar natures. As exemplified cases, we produce inorganic, metallic silver fibres from solution-based reactive synthesis; and organic conducting PEDOT:PSS (poly(3,4-ethylenedioxythiophene) polystyrene sulfonate) fibres, which is of special interest for biological applications considering the difficulty in producing functional PEDOT:PSS fibres of diameters below the typical cell size (a few microns). In this context, we have exploited the distinctive and versatile functional advantages of the fibre array, namely: permissiveness, directionality and high surface area-to-volume ratio, in applications covering flow-permissive humidity sensor, and bio-impedimetric sensor. We then explore novel circuitry architecture afforded by the iFFP process, presenting the concept of 3D ‘floating electronic architectures’, and merging organic and inorganic fibre materials in the same transparent conductive network.

Results

Inflight fluidic fibre printing

The iFFP process is schematically shown in **Fig.1 A**. Silver (Ag) or PEDOT:PSS are used as the fibre materials; with Ag being a widely used conducting metal (28), and PEDOT:PSS a biocompatible conducting polymer, with applications ranging from textile (29, 30), printed electronics (31, 32), to bio-interfacing structures (33, 34). In order to reflect the universality of the process, we derive fibres from readily available aqueous solutions of low viscosity (~10-60 mPa·s). For Ag, we demonstrate reactive synthesis of fibres from a modified Tollens’ solution

containing an Ag salt and a reducer (35). This differs from commonly used metal nanoparticle-based conducting inks in fibre production processes that are generally prepared by mixing metal nanoparticles with polymers. For PEDOT:PSS fibres, a commercial aqueous colloidal solution is used (see Materials and Methods).

The iFFP process utilises a core-shell nozzle, delivering an aqueous sizing agent in the sheath (polyethylene oxide, PEO, $M_w = 4$ MDa, 2% w/w in DI water) to ensure the core continuity and prevent interface instability. Sub-100 °C heating is applied to rapidly evaporate the solvent, and to simultaneously activate the Ag precursor in the case of Ag fibre production. The iFFP technique does not require pre-processing or additives to tune the viscosity of the core solution, as the fibre structure can be transiently maintained by the sizing polymer in the sheath during fibre synthesis. This differs from usual printing techniques in which the viscosity of inks needs to be optimized beforehand (36, 37); hence our technique supports a variety of functional materials to be directly used in their original forms as the fluid core.

At the initial stage of fibre synthesis, the core-shell nozzle is positioned at ~ 100 μm above the surface of the heated contact pad, initially forming a droplet that becomes a fibre bond, and then the stage translation leads to capillary breakup of the droplet to initiate a fibre. The fibre is produced by both the mechanical stretching and the heating that ensures solvent evaporation where the core solution will eventually solidify into the conductive phase for both Ag and PEDOT:PSS fibres (**Fig.1 A**). Subsequently, the fibre reaches the opposite contact pad and forms another fibre bond, bridging the two electrodes. **Figure.1 B** shows a picture of the resulted suspended fibre array, on which an LED light is suspended with a dandelion seed. The ultrathin diameter of iFFP fibres makes the array appears to be visually transparent, even comparing with the fine hairs of the dandelion. Due to the substrate-free nature of the fibre array, the hairs and stem of the seed pass freely through the fibre array while being supported, showing the permissiveness of iFFP fibre array. This suspended electrical conduit illustrates both the

transparency and conductivity of the fibre array. Alternatively, the fibre arrays can be combined to form a network structure, in which the fibre materials can be varied in different tiers of the same grid. In iFFP, the freshly printed fibres exhibit a transient semi-liquid state, which can be exploited for controlling the crossing points in the grid, to be structured as a non-junctioned or junctioned network. For instance, if the second tier of fibres solidify independently without interacting with the first fibre tier, the crossing points remain non-junctioned (**Fig.1 C**). By applying a low electrical field (200 V.cm^{-1}) at the nozzle (**Fig.1 D**) when printing the second fibre tier, the fibres would be pulled down slightly to merge with the first tier before solvents evaporation, resulting in a junctioned fibre grid structure.

The fibre bonds (**Fig.1 E**) serve the electrical connection between the fibre and the electrical contact pads. The direct connection between the electrical pad and the conducting phase (*e.g.* Ag) of the fibre bond, with minimal interference of the PEO sizing polymer, is evidenced by X-ray photoelectron spectroscopy (XPS) depth profiling (**Fig.1 F**). An ion gun is used to etch the fibre bond and Cu contact pad junction area in the depth direction, and XPS high resolution spectra of Silver 3d and Carbon 1s are acquired at each etching layer. At all depth layers, main peaks at 368.3 eV and 374.3 eV correspond to Ag 3d $5/2$ and Ag 3d $5/3$ binding energies, and the main peak at 284.7 eV corresponds to C 1s (C-C) binding energy (19) (**fig. S1**). Due to the complexity of the materials at the junction area, it is not straightforward to estimate the precise etching distance from the etching time and energy. However, given that the electrical contact pad is made of copper, the Cu 2p intensity values at each layer were used to provide an estimation of the distance between the current etching layer and the copper electrode. We should mention that the ion beam diameter ($\sim 100 \text{ }\mu\text{m}$ wide) is much larger than the fibre bond ($\sim 60 \text{ }\mu\text{m}$ wide), explaining why Cu 2p peak is detected in all layers during the XPS depth analysis. At layer 0, the top surface of the fibre bond, the silver intensity is weak while the carbon intensity is strong, meaning that the surface of the fibre bond is mainly covered by PEO. When etching down the

junction, the silver intensity starts to increase and the carbon intensity keeps decreasing, indicating that the silver is mainly covered underneath the PEO. The copper intensity reaches its maximal value at around layer 19, meaning the surface of the copper electrode contact pad has been reached. The fact that Carbon content decreases monotonically from the top of the fibre bond to the surface of the copper electrode pad suggests that there is no polymer-rich barrier between the silver phase and the copper electrode contact pad. The XPS depth profiles support that silver is directly in contact with the copper electrode contact pad and thus to guide the conducting phase, forming a continuous electrical pathway from the electrical contact pads to the fibres.

Aided by the sizing polymer to form the sheath of the iFFP fibres, the core phase of fibres only consists substances of the silver precursor solution, without an inter-penetrating polymer that binds and separates the synthesized silver particles. Therefore, the critical temperature required to obtain a connected metallic core in our system is expected to be controlled by the initiation temperature of silver reaction and solvent evaporation ($\sim 60\text{-}80\text{ }^{\circ}\text{C}$), rather than by the calcination temperature ($> 250\text{ }^{\circ}\text{C}$) of the polymer binder as reported in previous studies (*11, 19*). Using iFFP, we demonstrate that a one-step process at sub- $100\text{ }^{\circ}\text{C}$ is sufficient to obtain adequate fibre conductivity (see next section), in comparison with usual fibre production techniques that require post-processing such as sintering (*11, 19*). Moreover, as iFFP proceeds at a temperature lower than $100\text{ }^{\circ}\text{C}$, this would create opportunities for the direct integration of both PEDOT:PSS and silver-based fibres into a wider range of materials and structures. The iFFP process is foreseen to be most suitable for applications that require reduced temperature and mild fabrication environments, such as for incorporating biologic factors and thermo-sensitive materials.

Morphological and opto-electro-mechanical properties of iFFP fibres

Typical micrographs of aligned, suspended conducting fibre arrays are shown in **Fig.1 G-H**. Such an array of around 100 fibres can be printed within one minute, thanks to the high printing speed (600 mm/s). This makes iFFP an efficient fibre printing process. Fibre diameter typically ranges from 1-3 μm ($2 \mu\text{m} \pm 0.7 \mu\text{m}$). For both Ag and PEDOT:PSS fibres, SEM micrographs show a smooth surface texture, as shown in the insert of **Fig.1 H**. Alternatively, the iFFP process can print fibres of different patterns, as illustrated by the optical image of suspended cross-junctioned fibre network shown in **Fig.1 I**. In addition, by applying a small voltage at the nozzle ($\sim 150 \text{ V}$), fibres can be bound onto different substrate surfaces of either conducting or insulating nature (**fig. S2**), demonstrating flexible switch between ‘spanning’ to ‘on-substrate’ printing.

TEM and EDX micrographs of an Ag fibre are shown in **Fig.1 J**. The TEM micrograph shows a solid, continuous core of silver (appears white in the image due to stronger diffraction from the heavier compounds), surrounded by a thin sheath of PEO (appears translucent due to lighter organic compounds). The TEM image also reflects the continuity of the core in the longitudinal direction. Chemical mapping by EDX (Energy-dispersive X-ray) of Ag-PEO fibre on the bottom side of **Fig.1 J** further confirms that the core is dominated by silver species, while the shell is dominated by carbon species that represent the PEO polymer. Further investigations of the Ag fibre composition using TGA (thermogravimetric analysis) have been performed to estimate the mass fraction of silver content (**Fig.2 A**). The weight loss of around 7 % from 300 °C to 400 °C can be attributed to the thermal decomposition of PEO, which is verified by using pure PEO fibres as reference. Above 400 °C, there is no significant weight loss due to the high thermal stability of silver content in the solidified Ag precursor. This indicates that Ag-PEO fibres have over 90 % w/w of silver content. X-ray diffraction results of the Ag-PEO fibres (**fig. S3**) support the presence of normal silver crystal phases associated with elemental silver. In other

words, when printing fibres at sub-100°C, the majority of the silver precursors has been converted to elemental silver in the fibre core.

In order to evaluate the mechanical properties of the suspended fibre array, tensile test is performed on suspended Ag, PEDOT:PSS and pure PEO fibres (**Fig.2 B**). Both Ag and PEDOT:PSS fibres exhibit Young's modulus and tensile strength lower than their pure core phase counterparts. This is as expected since the PEO sizer has a low Young's modulus (~2 MPa) and yield strength (~5 MPa), and the overall mechanical properties of the fibres are determined by both the PEO sizer and the core materials. As observed in **Fig.2 B**, for Ag fibres, the yield strength and Young's modulus in the elastic regime are $E \sim 10$ MPa and $\sigma_y \sim 15$ MPa, respectively. It is noteworthy that these values are similar to the mechanical properties of human skin (38). The yield strength of PEDOT:PSS fibre is ~30 MPa and the Young's modulus is ~150 MPa. Instead of having binder polymers intercalating the conducting phases inside a fibre, a core-shell structure could achieve unique mechanical properties without compromising the fibre conductivity.

In the case of Ag fibres, $\sim 10^6$ S.m⁻¹ bond-to-bond fibre conductivity is obtained under a processing temperature of 80 °C. **Figure.2 C** shows that the conductivity and fabrication temperature of Ag fibres obtained by iFFP compare favourably with those of existing literature. In particular, our data directly reflects the bond-to-bond fibre conductivity, having encompassed the contact resistance normally incurred in a device setting. With regards to the PEDOT:PSS fibres, a bond-to-bond conductivity of about 400 S/m is obtained at ~65 °C. Overall, the iFFP technique produces fibres of good conductivity at low processing temperatures (<100 °C). Since iFFP can produce thin spanning fibres, the 'substrate-free' conducting fibre arrays even have better transparency compared with a standard transparent conductor film, *i.e.* ITO/PET (Indium Tin Oxide coated Polyethylene Terephthalate) with similar directional conductance (**Fig.2 D**). At a fibre density of 20 fibres/mm, the suspended Ag fibre array exhibit over 95 % transmittance in the 350-700 nm regime. The benefits in enhancing light transmission is especially obvious for the

near-UV (below 400 nm) region, where the transmittance of the commonly used transparent films decreases sharply (see **fig. S4** for absorption coefficient *versus* wavelength). The opto-electrical property of the suspended iFFP fibre array makes them suitable for fulfilling applications where UV spectral region is involved (39).

Flow-permissive fibre sensor

Along with favourable opto-electrical characteristics, the suspended feature of the iFFP fibre array provides unique advantage of being permissive to fluid flow. In this context, we have exploited the PEDOT:PSS fibre array as a sensing electrode for detecting spatiotemporal dynamics of moisture flows. In comparison with conventional fibre-based moisture sensing materials (40), the iFFP PEDOT:PSS fibre relies on measuring the end-to-end fibre resistance evolution, thus allowing tailored signal read-out dependent on the fibre organisation. **Figure.3 A** shows that the fibre resistivity increases linearly with respect to the relative humidity from 55 % to 90 % at room temperature (as calibrated with a hygrometer, Onecall, 1784721). Compared to a regular commercial sensor (HIH-5031-001, Honeywell), the iFFP fibres demonstrate a faster response (~100 ms time resolution *versus* ~500 ms), as shown by the detection onset (~500 ms faster) and decay at maximal humidity value (~4 s faster) upon the impingement of a pulse humid mist (**Fig.3 B**). Therefore, the small diameter, high surface-area-to-volume, and substrate-free configuration of the iFFP fibres may aid moisture absorption and desorption, enabling the fibres to promptly equilibrate with the surrounding humidity. Since the fibre resistance values always return to the baseline value after removal of the mist, the influence of moisture absorption on fibre resistivity is a reversible process. With this capability, the dynamics of moisture flow can be monitored by using a stacked fibre array in a 3D configuration where the moisture flow can freely pass through the fibre arrays (**Fig.3 C**), and the spatiotemporal resolution of detection is defined by the distance between two adjacent tiers of fibre arrays. Typically, a pulse mist applied from the bottom rises to encounter with level-1 to level-3 sensing tiers sequentially. Simultaneously,

imaging of the flow dynamics can be performed considering the transparent characteristic of the multi-tier fibre-based electrodes. The time-resolved fibre resistance at each sensing tier is recorded as represented in **Fig.3 D**. The onset of resistance change has a time delay between subsequent sensing tiers of about ~ 1 s, corresponding well to the flow dynamics captured with a high-speed camera (**Fig.3 E**). This confirms the responsiveness and sensitivity of the spatiotemporal dynamic sensing. We should mention that the contrast of the mist in the processed images are due to in- and out- camera focus differences and does not reflect the water concentration distribution.

PEDOT:PSS fibre-based biointerface devices

PEDOT:PSS are known to have convenient cellular biocompatibility (30, 40, 41). Thus, we have used the fibre array to form bio-interfaced sensing devices. We demonstrate that the PEDOT:PSS fibre array retains their designated patterns and orientation post-liquid immersion, and remains visually stable in cell culture media for at least 3 days (**fig. S5**). In addition, it has been shown that PEDOT:PSS electrodes remain stable in cell culture media over a period of several month for *in vitro* electrophysiology applications (43). Upon cell seeding, the PEDOT:PSS fibres are shown to facilitate spontaneous cell attachment, and viable cell culture (viability over 3 days based on U87 cell test, **fig. S6**). The high aspect ratio and small diameter of the fibres provide topographical guidance to the cells. As shown in **Fig.4 A, B and C**, 3T3 cells (fibroblast cells from mouse) follow the aligned fibre patterns over the entire fibre array. Different orientations of the fibres ($0^\circ/90^\circ$, $0^\circ/60^\circ$, and 0°) guide the cells to align with respect to the fibre patterns, as highlighted in the associated histograms. To extend this capability further, we produce centimetre long fibres to guide cellular alignment, where the fibre can simultaneously function as an impedimetric sensor detecting dynamics of cell coverage (**Fig.4 D**). Cell coverage on PEDOT:PSS electrode surfaces is known to increase the electrode's sensing impedance (41, 42). Coupled with simultaneous live cell imaging permitted by the fibre array, it is found that in our fibre-electrode setup, the

impedance increases most noticeably during the initial stages of cell attachment and fibre-guided cell alignment (within approximately 100 min from cell sedimentation). **Figure.4 E** shows the impedance spectrum series of a typical time-lapse study; where **Fig.4 F** plots the impedance sampled at 10 kHz, of which evolution could be cross-correlated to the cellular dynamics data captured by time-lapse imaging in **Fig.4 G** and **video S1**.

Creating circuit architectures using iFFP fibres

The free-form nature of the iFFP suspended conducting fibre arrays enables unconventional architectures harnessing its unique opto-electro-mechanical properties. As proof of concepts, we have fabricated 3D-layered ‘floating electronics’ and suspended cross- (homo- and hetero-) junctioned fibres that cannot be easily achieved by existing fibre fabrication or even printing techniques.

For example, LEDs can be directly powered through the transparent fibre electrode without soldering. Since the PEO sizer is only present as a thin sheath, and has a low breakdown potential (44), the fibre array can be readily used as electrical conduits. **Figure.5 A, B and C** show the simple successive steps to connect the LED circuit on the suspended Ag fibre array, where the LED light can be powered (~10 V). Fibre array is mechanically strong enough to not only support the weight of the LED light, but also to bear the impact force when the light is placed on the fibre array. Since iFFP can produce thin spanning fibres, the ‘substrate-free’ conducting fibre arrays are noticeable more transparent by eliminating substrate-absorption and minimising the level of oblique light reflection compared with a standard transparent conductor film, *i.e.* ITO/PET with similar directional conductance (**Fig.5 D-E**). ‘Floating LED circuit’ is created as demonstrated by the in- and out-focus images in **Fig.5 F-G**. Furthermore, the sub-100 °C fabrication process of iFFP enables fibre array to be directly integrated onto materials with low melting temperatures, such as commonly used 3D printing plastics. This opens the way to low-cost and easily assembled 3D-layered ‘floating circuit’, as evidenced in **Fig.5 H** and **fig. S7**. Similarly, spanning

PEDOT:PSS fibre array can also be used to connect and support multiple LED lights on the same array (shown in the insert in **Fig.5 H**).

At the few micron-scale, creating hetero-junction between organic and inorganic fibres is especially challenging when considering the very dissimilar processing conditions normally involved in manufacturing these fibres. However, the versatility fluidic printing feature of our processing technique enables materials of different nature to be *in-situ* integrated into the same fibre network in a grid structure (see fabrication principle introduced in **Fig.1 C-D**). A typical suspended, hetero-junctioned fibre network of Ag and PEDOT:PSS fibres is sketched and shown by global SEM in **Fig.6 A**. Zoomed-in SEM image at the junction point and EDX maps in **Fig.6 B** show the well-integrated PEDOT:PSS and Ag junction. The merging at the cross-junctions happens when the second tier of semi-liquid fibres comes to contact with the first tier of fibres, making this an *in-situ* process working at sub-100 °C. Additionally, homo-junctioned (Ag-Ag or PEDOT:PSS-PEDOT-PSS) fibres can also be produced as shown in **Fig.6 C-D**. On the other hand, iFFP offers the possibility to create non-junctioned fibre network (**fig. S8**). Reducing contact resistance at crossing fibre junctions still exists as a technical challenge for producing percolating conductive networks (45). Post thermal treatment or mechanical pressing that are commonly used to merge fibre junctions have some limits (46, 47). Indeed, these methods can damage the fibres and, especially, cannot be applied for processing suspended fibres that are of a few micron width. Thus, iFFP is a unique and versatile method to create inorganic/organic cross-junctioned network without additional post-processing. The ability of iFFP to design fibre networks of different junction types, using different materials, may pave the way towards making transparent fibre-logic circuits (48).

Discussion

We have provided a first insight into a new way of producing substrate-free fibre arrays using an original one-step approach, mitigating additional post-processing that usually behave to

conventional fibre printing processes. Inflight Fluidic Fibre Printing (iFFP) offers rapid and low-cost fabrication of high-performance transparent conducting fibres with minimised contact resistance and surface resistivity. The iFFP fibre array can be directly coupled with materials of low operation temperatures ($< 100\text{ }^{\circ}\text{C}$), starting from solutions or dispersions of low viscosity fluids.

We have demonstrated the universality of iFFP in producing PEO-sheathed fibres made of metal (Ag) and conducting polymer (PEDOT:PSS) respectively. Both Ag and PEDOT:PSS fibres exhibit good bond-to-bond fibre conductivities. By readily fabricating an in-plane array of fibres and assembling them into 3D architectures, iFFP multiplies the conduction ability of single fibres while still harnessing the superior optical transparency through single fibre thicknesses. With this capability, all the fibre sensor structures presented in this work have supported convenient imaging acquisition, which is important for data validation, and also enabling future potentials in multi-parametric studies of process dynamics. When constructed as a moisture sensor, suspended PEDOT:PSS fibre array is ~ 4 times more responsive than the conventional film-based sensing devices due to the fibres' small unit-volume and high surface-to-area-ratio. Further, a layer-by-layer 3D fibre array permits the spatiotemporal flow dynamics to be captured, which is not possible with existing film-based sensors. The versatile and facile device-integration also inspires new concepts in circuitry architectures. Using the superior optical transparency and minimal reflection of the substrate-free fibres, we demonstrated, for the first time, 3D-layered 'floating electronics'. In addition, we constructed suspended fibre networks of homo- or hetero- fibre cross-junctions. Thus, by expanding the material combinations in the future, the iFFP process is foreseen to offer a tool to fabricate conducting fibres with tuneable combination of mechanical, optical and electrical properties, broadening the property scopes offered by existing transparent conducting fibre and network structures. The iFFP process has brought new functional dimensions to the small-diameter conducting fibre structures. We envisage these distinctive forms

of transparent fibre array and networks to be exploited in emerging fields from bioelectronics to 3D electronics.

Materials and Methods

Solution preparation

The reactive Ag ink was prepared with modified Tollens' ink (35): 1 g Ag acetate (216674, Sigma-Aldrich) was dissolved in 2.5 mL ammonium hydroxide (28% NH₃, Alfa Aesar), then 0.2 mL formic acid (Thermo Fisher Scientific) was added, followed by 3 hr stirring at room temperature to obtain a transparent solution. PEDOT:PSS solution was prepared by mixing 95% vol./vol of PEDOT:PSS (Heraeus Clevios™ PH 1000) and 5% vol./vol of ethylene glycol (Sigma-Aldrich). The solution was sonicated for around 20 minutes and then filtered through 1.2 µm PTFE (Polytetrafluoroethylene) filter before using. In order to enhance the structure and conductivity stability of PEDOT:PSS fibres in the case of using them inside cell culture media, 1 % w/w of DVS (Divinylsulfone, Sigma-Aldrich) was then added to the solution as a cross-linker. DVS is able to cross-link PEDOT:PSS under room temperature and the cross-linked PEDOT:PSS is proven to be biocompatible. After mixed with DVS, the solution was mixed carefully and filtered through a 1.2 µm PTFE filter. PEO (Mw = 4M Da) was dissolved in DI water at 2% w/w and stirred at room temperature for 24 hours.

iFFP of fibre array

The iFFP set-up consisted of two X-Y translation stages (DDSM100/M, Thorlabs) for fibre printing and a Z stage (L490MZ/M, Thorlabs) to adjust the distance between the nozzle and the contact pad. The core-shell nozzle was assembled by inserting a micropipette-filling capillary (ID 100 µm and OD 164 µm, World Precision Instrument) into a 22 gauge blunt end stainless steel needle. The nozzle was kept at a fixed position. Two pumps (AL-1000, World Precision Instruments) were used to deliver the PEO sizing solution and functional core solutions into the sheath and core channels of the core-shell nozzle respectively via 0.8 mm inner diameter tubings.

The sheath solution flow rate was maintained at $\sim 50 \mu\text{L/hr}$ for the injection of the PEO sizing solution, and the core flow rate was maintained at $\sim 25 \mu\text{L/hr}$ for the injection of functional solutions. A heating plate was attached to the bottom of the translation stage and was continuously heated at 80°C for Ag fibre production and 65°C for PEDOT:PSS fibre production to assist reduction reaction and solvent evaporation. During the fibre printing process, the translation stage moved at a speed of 600 mm/s , and the distance between two electrical contact pads, which is fibre length, could be varied between 1 to 10 mm. In the process of printing fibres bond to a surface of substrates, a small voltage ($\sim 150 \text{ V}$) was applied on the tip of the nozzle in order to pull the printed fibres down to adhere to the substrates. The distance between the tip of the nozzle and the surface of the substrate was maintained at $\sim 5 \text{ mm}$.

Fibre characterisation

XPS spectra of the electrical contacting pad area for silver fibres was collected by ESCALAB 250Xi Photoelectron Spectroscopy with monochromatic Al $K\alpha$ -excitation (1486.68 eV), and a depth profile was conducted to acquire information of different depth layer (Ar^+ ion gun, 2000 eV). The analysis area was around $100 \mu\text{m}$. UV-VIS spectra were collected by Cary 7000 Universal Measurement Spectrophotometer (Agilent Technologies) with suspended fibre array samples, and the fibre density used for the measurement was 20 fibres/mm . The XRD measurement for silver fibres was carried out by Siemens D500 (SIEMENS). During the XRD measurement, silver fibres and silver ink were deposited onto separate microscope cover slides. TGA measurement was performed by TA Instruments Q500 TGA machine, with a heating rate of 10°C/minute under nitrogen environment. The stress-strain behaviour of fibres were measured on samples with an array of fibres (around 100 fibres per sample). Since suspended fibres are substrate-free and extremely thin, the conventional tensile test machine was not suitable. A self-assembled tensile rig was used as illustrated in **Fig.2 B**. Fibres were pulled up in the middle by a

probe, which was connected to a force sensor. The pulling force and displacement were recorded and later converted into stress and strain of the fibre according to the following equation.

$$strain = \frac{2\sqrt{D^2 + (L/2)^2} - L}{L} \times 100\%; \quad stress = \frac{F}{2 \cdot \cos(\alpha/2) \cdot A}$$

Where D is the displacement of the probe, L is the original fibre length, F is the force measured by the probe, α is the angle of the fibre at the tip of the probe and A is the original cross-section area of the fibre.

Fabrication of PEDOT:PSS fibre sensors

In the PEDOT:PSS moisture sensor, a commercial humidifier was used as the mist source, and multimeters (Keysight 34465A) were used to record the resistance change. High-speed camera (PHANTOM VEO-E 310L) was used to image the moisture flow. For fabricating cell interfacing devices, PEDOT:PSS fibres of 20 mm length were printed onto glass slides with patterned gold electrode (CRESTEC CABL 9000C E-Beam Lithography System). All samples were kept in room temperature for 24 hours before immersing into cell culture media, in order to make sure the completion of cross-linking process. The device was then sterilized under UV radiation for 30 minutes. Afterwards, the device was washed three times by PBS and incubated in cell culture media for 48 hours to remove excessive PSS in the fibres, and the media was refreshed before cell seeding. Fibroblasts cells (3T3) were seeded on the device, with the impedance spectrum sampled by PalmSens4 Potentiostat along with *in-situ* imaging (Leica confocal, SP5). Fluorescent images in **Fig.4 A, B and C** with phalloidin and DAPI stains were taken by fixing cells at 8 hours, and cell orientations were analysed using CellProfiler 2.3.

Cell viability assay with PEDOT:PSS fibres

Human glioblastoma cells, U-87 (ATCC), were cultured in Dulbecco's Modified Eagle's Media (DMEM, Invitrogen) supplemented with 10% Fetal Bovine Serum (FBS, Sigma-Aldrich) under 5% CO₂ at 37 °C incubation. Cells were seeded from a centrifuged cell pellet directly on fibres.

For the viability study, a seeding volume of 10 μL of cell pellet was used for each sample; samples were cultured for 3 days and imaged with optical microscopy. A live dead assay (Invitrogen) was performed following manufacturer's protocol on day 3, and imaged with Leica SP5 confocal microscope.

H2: Supplementary Materials

fig. S1. XPS high-resolution results of depth profiling on fibre bond area.

fig. S2. Versatility of IFD technique in printing fibres onto various substrates.

fig. S3. XRD on heated silver precursor droplet and Ag fibre.

fig. S4. Absorbance of Ag, PEDOT:PSS fibres, PEN and ITO-PET films in the 350-750 nm region.

fig. S5. PEDOT:PSS fibres stability post-liquid immersion.

fig. S6. Cell viability assay on PEDOT:PSS fibres.

fig. S7. 3D fibre based circuit configuration and LED lights placed on top of PEDOT:PSS fibre arrays.

fig. S8. Non-junctioned fibre grid.

video S1. Time-lapse imaging showing cell attachment onto PEDOT:PSS fibre arrays in the first 5 hours after seeding.

References and Notes

1. W. Zeng, L. Shu, Q. Li, S. Chen, F. Wang, X. M. Tao, Fiber-based wearable electronics: A review of materials, fabrication, devices, and applications. *Adv. Mater.* (2014), , doi:10.1002/adma.201400633.
2. S. Yao, Y. Zhu, Nanomaterial-enabled stretchable conductors: Strategies, materials and devices. *Adv. Mater.* **27** (2015), pp. 1480–1511.
3. T. Sannicolo, M. Lagrange, A. Cabos, C. Celle, J. P. Simonato, D. Bellet, Metallic Nanowire-Based Transparent Electrodes for Next Generation Flexible Devices: a Review. *Small*. **12** (2016), pp. 6052–6075.
4. S. Kang, S. Cho, R. Shanker, H. Lee, J. Park, D. S. Um, Y. Lee, H. Ko, Transparent and conductive nanomembranes with orthogonal silver nanowire arrays for skin-attachable loudspeakers and microphones. *Sci. Adv.* (2018), doi:10.1126/sciadv.aas8772.
5. D. Ye, Y. Ding, Y. Duan, J. Su, Z. Yin, Y. A. Huang, Large-Scale Direct-Writing of Aligned Nanofibers for Flexible Electronics. *Small* (2018), , doi:10.1002/smll.201703521.
6. B. Sciacca, J. Van De Groep, A. Polman, E. C. Garnett, Solution-Grown Silver Nanowire Ordered Arrays as Transparent Electrodes. *Adv. Mater.* (2016), doi:10.1002/adma.201504045.
7. Y. Koizumi, N. Shida, M. Ohira, H. Nishiyama, I. Tomita, S. Inagi, Electropolymerization on wireless electrodes towards conducting polymer microfibre networks. *Nat. Commun.* **7** (2016), doi:10.1038/ncomms10404.
8. P. C. Hsu, S. Wang, H. Wu, V. K. Narasimhan, D. Kong, H. Ryoung Lee, Y. Cui, Performance enhancement of metal nanowire transparent conducting electrodes by mesoscale metal wires. *Nat. Commun.* (2013), doi:10.1038/ncomms3522.
9. M. Park, J. Im, M. Shin, Y. Min, J. Park, H. Cho, S. Park, M. B. Shim, S. Jeon, D. Y. Chung, J. Bae, J. Park, U. Jeong, K. Kim, Highly stretchable electric circuits from a composite material of silver nanoparticles and elastomeric fibres. *Nat. Nanotechnol.* (2012), doi:10.1038/nnano.2012.206.
10. X. Bai, S. Lin, H. Wang, Y. Zong, H. Wang, Z. Huang, D. Li, C. Wang, H. Wu, Room-temperature processing of silver submicron fiber mesh for flexible electronics. *npj Flex. Electron.* (2018), doi:10.1038/s41528-017-0016-7.
11. Y. Huang, X. Bai, M. Zhou, S. Liao, Z. Yu, Y. Wang, H. Wu, Large-Scale Spinning of Silver Nanofibers as Flexible and Reliable Conductors. *Nano Lett.* (2016), doi:10.1021/acs.nanolett.6b02654.
12. S. Lee, S. Shin, S. Lee, J. Seo, J. Lee, S. Son, H. J. Cho, H. Algadi, S. Al-Sayari, D. E. Kim, T. Lee, Ag nanowire reinforced highly stretchable conductive fibers for wearable electronics. *Adv. Funct. Mater.* (2015), doi:10.1002/adfm.201500628.
13. Y. Lu, J. Jiang, S. Yoon, K. S. Kim, J. H. Kim, S. Park, S. H. Kim, L. Piao, High-Performance Stretchable Conductive Composite Fibers from Surface-Modified Silver Nanowires and Thermoplastic Polyurethane by Wet Spinning. *ACS Appl. Mater. Interfaces* (2018), doi:10.1021/acsami.7b16022.
14. Z. Xu, Z. Liu, H. Sun, C. Gao, Highly electrically conductive Ag-doped graphene fibers as stretchable conductors. *Adv. Mater.* (2013), doi:10.1002/adma.201300774.
15. L. Li, L. Pan, Z. Ma, K. Yan, W. Cheng, Y. Shi, G. Yu, All Inkjet-Printed Amperometric Multiplexed Biosensors Based on Nanostructured Conductive Hydrogel Electrodes. *Nano Lett.* **18**, 3322–3327 (2018).
16. A. D. Valentine, T. A. Busbee, J. W. Boley, J. R. Raney, A. Chortos, A. Kotikian, J. D. Berrigan, M. F. Durstock, J. A. Lewis, Hybrid 3D Printing of Soft Electronics. *Adv. Mater.* (2017), doi:10.1002/adma.201703817.
17. W. Zhou, S. Bai, Y. Ma, D. Ma, T. Hou, X. Shi, A. Hu, Laser-Direct Writing of Silver

- Metal Electrodes on Transparent Flexible Substrates with High-Bonding Strength. *ACS Appl. Mater. Interfaces* (2016), doi:10.1021/acsami.6b07696.
18. M. A. Skylar-Scott, S. Gunasekaran, J. A. Lewis, Laser-assisted direct ink writing of planar and 3D metal architectures. *Proc. Natl. Acad. Sci. U. S. A.* (2016), doi:10.1073/pnas.1525131113.
 19. Y. Lee, S. Y. Min, T. S. Kim, S. H. Jeong, J. Y. Won, H. Kim, W. Xu, J. K. Jeong, T. W. Lee, Versatile Metal Nanowiring Platform for Large-Scale Nano- and Opto-Electronic Devices. *Adv. Mater.* (2016), doi:10.1002/adma.201602855.
 20. X. Zhao, F. Chen, Y. Li, H. Lu, N. Zhang, M. Ma, Bioinspired ultra-stretchable and anti-freezing conductive hydrogel fibers with ordered and reversible polymer chain alignment. *Nat. Commun.* **9** (2018), doi:10.1038/s41467-018-05904-z.
 21. W. Lee, T. Someya, Emerging Trends in Flexible Active Multielectrode Arrays. *Chem. Mater.* **31**, 6347–6358 (2019).
 22. H. Fu, K. Nan, W. Bai, W. Huang, K. Bai, L. Lu, C. Zhou, Y. Liu, F. Liu, J. Wang, M. Han, Z. Yan, H. Luan, Y. Zhang, Y. Zhang, J. Zhao, X. Cheng, M. Li, J. W. Lee, Y. Liu, D. Fang, X. Li, Y. Huang, Y. Zhang, J. A. Rogers, Morphable 3D mesostructures and microelectronic devices by multistable buckling mechanics. *Nat. Mater.* **17**, 268–276 (2018).
 23. Y. Cheng, R. Wang, J. Sun, L. Gao, Highly Conductive and Ultrastretchable Electric Circuits from Covered Yarns and Silver Nanowires. *ACS Nano* (2015), doi:10.1021/nn5070937.
 24. R. Jalili, J. M. Razal, G. G. Wallace, Wet-spinning of PEDOT:PSS/functionalized-SWNTs composite: A facile route toward production of strong and highly conducting multifunctional fibers. *Sci. Rep.* **3** (2013), doi:10.1038/srep03438.
 25. C. Lu, S. Park, T. J. Richner, A. Derry, I. Brown, C. Hou, S. Rao, J. Kang, C. T. Moritz, Y. Fink, P. Anikeeva, Flexible and stretchable nanowire-coated fibers for optoelectronic probing of spinal cord circuits. *Sci. Adv.* **3** (2017), doi:10.1126/sciadv.1600955.
 26. H. Lu, D. Zhang, J. Cheng, J. Liu, J. Mao, W. C. H. Choy, Locally Welded Silver Nano-Network Transparent Electrodes with High Operational Stability by a Simple Alcohol-Based Chemical Approach. *Adv. Funct. Mater.* (2015), doi:10.1002/adfm.201501004.
 27. J. Choi, Y. S. Shim, C. H. Park, H. Hwang, J. H. Kwack, D. J. Lee, Y. W. Park, B. K. Ju, Junction-Free Electrospun Ag Fiber Electrodes for Flexible Organic Light-Emitting Diodes. *Small.* **14** (2018), doi:10.1002/sml.201702567.
 28. N. Matsuhisa, D. Inoue, P. Zalar, H. Jin, Y. Matsuba, A. Itoh, T. Yokota, D. Hashizume, T. Someya, Printable elastic conductors by in situ formation of silver nanoparticles from silver flakes. *Nat. Mater.* **16**, 834–840 (2017).
 29. A. K. Yetisen, H. Qu, A. Manbachi, H. Butt, M. R. Dokmeci, J. P. Hinestroza, M. Skorobogatiy, A. Khademhosseini, S. H. Yun, Nanotechnology in Textiles. *ACS Nano.* **10** (2016), pp. 3042–3068.
 30. J. D. Ryan, D. A. Mengistie, R. Gabrielsson, A. Lund, C. Müller, Machine-Washable PEDOT:PSS Dyed Silk Yarns for Electronic Textiles. *ACS Appl. Mater. Interfaces.* **9**, 9045–9050 (2017).
 31. N. Matsuhisa, M. Kaltenbrunner, T. Yokota, H. Jinno, K. Kuribara, T. Sekitani, T. Someya, Printable elastic conductors with a high conductivity for electronic textile applications. *Nat. Commun.* **6** (2015), doi:10.1038/ncomms8461.
 32. Y. Guo, M. T. Otley, M. Li, X. Zhang, S. K. Sinha, G. M. Treich, G. A. Sotzing, PEDOT:PSS “wires” Printed on Textile for Wearable Electronics. *ACS Appl. Mater. Interfaces.* **8**, 26998–27005 (2016).
 33. D. Khodagholy, J. N. Gelinas, T. Thesen, W. Doyle, O. Devinsky, G. G. Malliaras, G. Buzsáki, NeuroGrid: Recording action potentials from the surface of the brain. *Nat.*

- Neurosci.* **18**, 310–315 (2015).
34. T. R. Ray, J. Choi, A. J. Bandothkar, S. Krishnan, P. Gutruf, L. Tian, R. Ghaffari, J. A. Rogers, Bio-integrated wearable systems: A comprehensive review. *Chem. Rev.* **119** (2019), pp. 5461–5533.
 35. S. B. Walker, J. A. Lewis, Reactive silver inks for patterning high-conductivity features at mild temperatures. *J. Am. Chem. Soc.* (2012), doi:10.1021/ja209267c.
 36. M. S. Onses, E. Sutanto, P. M. Ferreira, A. G. Alleyne, J. A. Rogers, Mechanisms, Capabilities, and Applications of High-Resolution Electrohydrodynamic Jet Printing. *Small.* **11** (2015), pp. 4237–4266.
 37. Y. H. Jo, I. Jung, C. S. Choi, I. Kim, H. M. Lee, Synthesis and characterization of low temperature Sn nanoparticles for the fabrication of highly conductive ink. *Nanotechnology.* **22** (2011), doi:10.1088/0957-4484/22/22/225701.
 38. J. F. M. Manschot, A. J. M. Brakkee, The measurement and modelling of the mechanical properties of human skin in vivo-I. The measurement. *J. Biomech.* **19**, 511–515 (1986).
 39. C. M. Weber, D. M. Eisele, J. P. Rabe, Y. Liang, X. Feng, L. Zhi, K. Müllen, J. L. Lyon, R. Williams, D. A. VandenBout, K. J. Stevenson, Graphene-based optically transparent electrodes for spectroelectrochemistry in the UV-vis region. *Small.* **6**, 184–189 (2010).
 40. D. Liu, A. Tarakanova, C. C. Hsu, M. Yu, S. Zheng, L. Yu, J. Liu, Y. He, D. J. Dunstan, M. J. Buehler, Spider dragline silk as torsional actuator driven by humidity. *Sci. Adv.* **5** (2019), doi:10.1126/sciadv.aau9183.
 41. M. Marzocchi, I. Gualandi, M. Calienni, I. Zironi, E. Scavetta, G. Castellani, B. Fraboni, Physical and Electrochemical Properties of PEDOT:PSS as a Tool for Controlling Cell Growth. *ACS Appl. Mater. Interfaces.* **7**, 17993–18003 (2015).
 42. F. Santoro, Y. Van De Burgt, S. T. Keene, B. Cui, A. Salleo, Enhanced Cell-Chip Coupling by Rapid Femtosecond Laser Patterning of Soft PEDOT:PSS Biointerfaces. *ACS Appl. Mater. Interfaces.* **9**, 39116–39121 (2017).
 43. G. Dijk, A. L. Rutz, G. G. Malliaras, Stability of PEDOT : PSS-Coated Gold Electrodes in Cell Culture Conditions. **1900662** (2019), doi:10.1002/admt.201900662.
 44. N. Koizumi, T. Hanai, Dielectric Properties of Polyethylene Glycols Dielectric Relaxation in Solid State. *Bull. Inst. Chem. Res. Kyoto Univ.* **42**, 115–127 (1964).
 45. S. An, H. S. Jo, D. Y. Kim, H. J. Lee, B. K. Ju, S. S. Al-Deyab, J. H. Ahn, Y. Qin, M. T. Swihart, A. L. Yarin, S. S. Yoon, Self-Junctioned Copper Nanofiber Transparent Flexible Conducting Film via Electrospinning and Electroplating. *Adv. Mater.*, 7149–7154 (2016).
 46. W. Gaynor, G. F. Burkhard, M. D. McGehee, P. Peumans, Smooth nanowire/polymer composite transparent electrodes. *Adv. Mater.* **23**, 2905–2910 (2011).
 47. E. C. Garnett, W. Cai, J. J. Cha, F. Mahmood, S. T. Connor, M. Greyson Christoforo, Y. Cui, M. D. McGehee, M. L. Brongersma, Self-limited plasmonic welding of silver nanowire junctions. *Nat. Mater.* **11**, 241–249 (2012).
 48. M. Hamedi, R. Forchheimer, O. Inanäs, Towards woven logic from organic electronic fibres. *Nat. Mater.* **6**, 357–362 (2007).

Acknowledgements: We thank Mr Guokun Ma from Hubei University for technical support and Mr Alex Casabuena-Rodriguez from Engineering Department of Cambridge University for his support in SEM imaging. **Funding:** This work was supported by the Engineering and Physical Sciences Research Council (EPSRC, EP/M018989/1), and European Research Council (ERC-StG, 758865). W Wang and X Li were grateful for the support from Chinese Scholarship Council,

A.L.R. acknowledges support from the Whitaker International Scholars Program and the European Commission's Horizon 2020 Marie Skłodowska-Curie Individual Fellowship (No. 797506), M.G thanks the funding from Cancer Research UK (CRUK), T.E.N thanks the funding from EPSRC Cambridge NanoDTC (EP/L015978/1). **Author contributions:** W.W and Y.Y.S.H conceived and designed experiments. W.W conducted fibre spinning and characterizations. K.O assisted with moisture sensor fabrication. A.L.R, X.L and G.G.M provided guidance and assisted in bio-impedimetric electrode production. M.G and T.E.N conducted cell culture experiments. W.W, Y.Y.S.H and K.O wrote the paper. All authors discussed results, and commented the manuscript. **Competing interest:** The authors declare that they have no competing interests. **Data and materials availability:** Extended data, software and materials in the main text and supplementary information are available upon request by contacting the corresponding author.

Figures and Tables

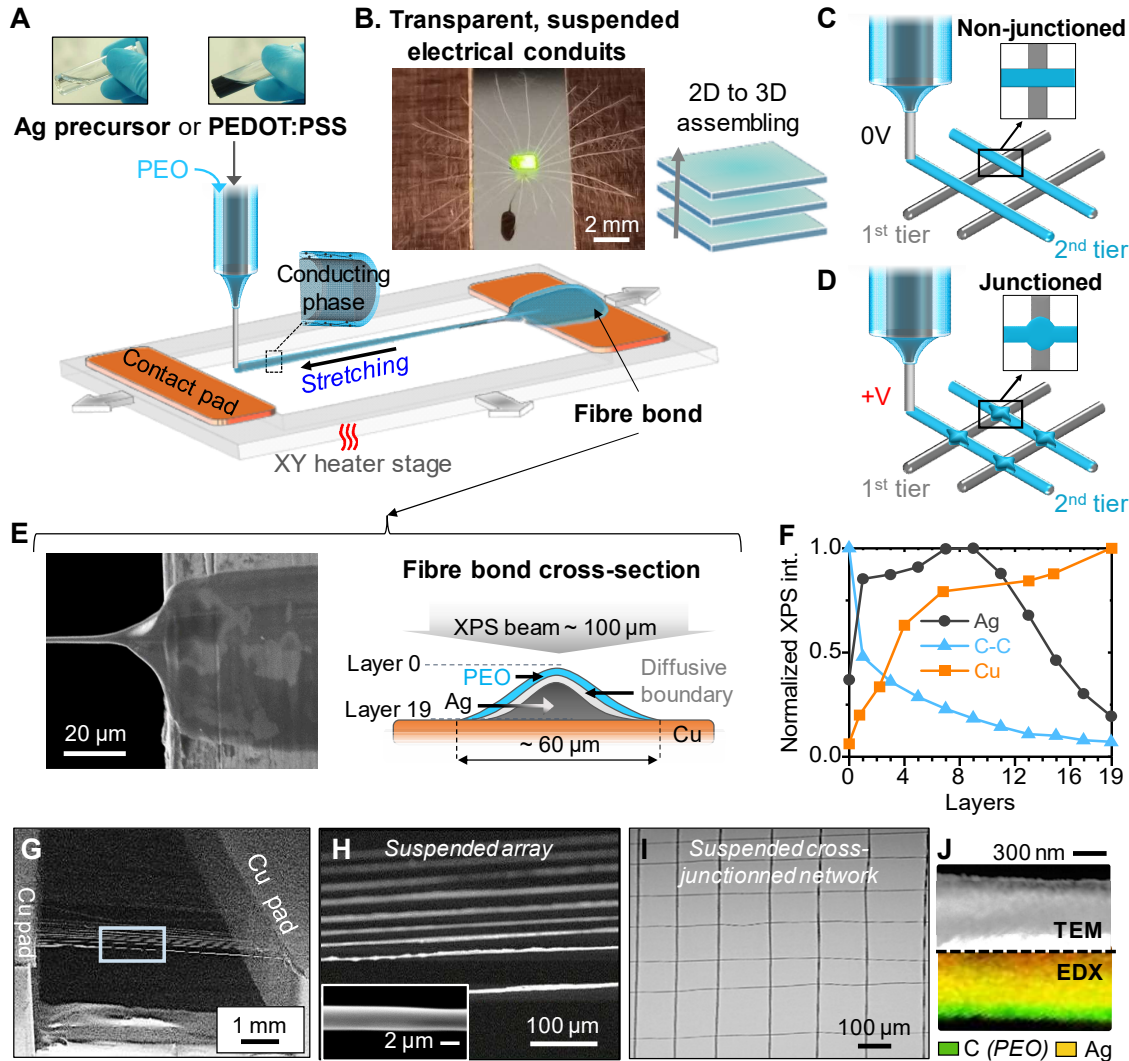


Fig. 1. iFFP fabrication of suspended fibre structures with *in-situ* bonding (A) Schematic of iFFP process for Ag and PEDOT:PSS fibres. (B) Image of a powered LED light and a dandelion seed on top of a suspended PEDOT:PSS fibre array, with the seed passing through the fibre array. (C-D) Schematics of non-junctioned and junctioned fibre grid structures. (E) SEM image showing fibre bond from top-view, and a cross-section schematic of fibre bond. (F) XPS depth profiling on Ag fibre bond. (G-H) SEM images of typical suspended, aligned fibre array. (I) Optical image of suspended iFFP fibre network. (J) TEM and EDX of a single Ag fibre.

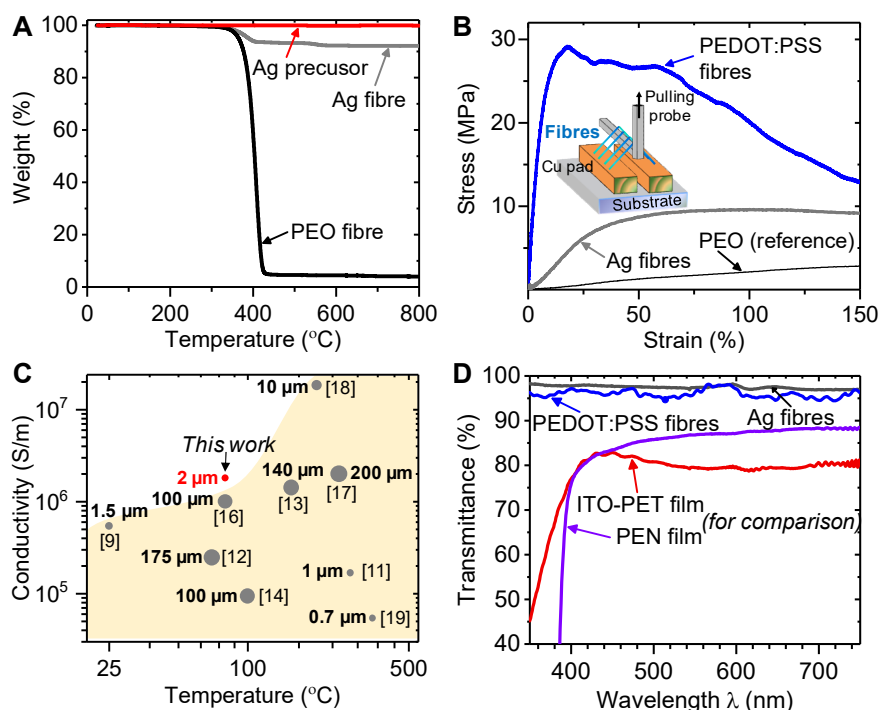


Fig. 2. Opto-electro-mechanical characteristics of iFFP fibre array. (A) TGA of Ag fibres, with pure PEO fibres and solidified Ag precursor as references. (B) Stress-strain curves of Ag, PEDOT:PSS and pure PEO fibres. (C) Summary of Ag fibre performance comparing processing temperature, conductivity and fibre diameter with literature (the ● symbol size is proportional to the fibre diameter or feature width). (D) Transmittance of Ag fibre array, PEDOT:PSS fibre array, PEN (Polyethylene Naphthalate) and ITO/PET (Indium Tin Oxide coated Polyethylene Terephthalate) films *versus* wavelength.

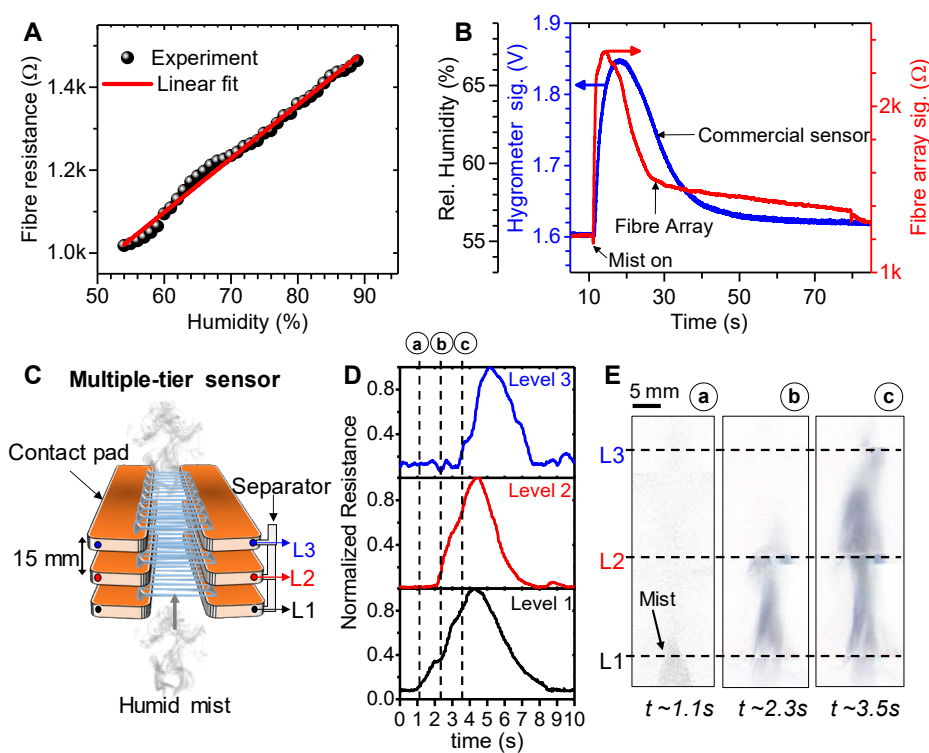


Fig. 3. Flow-permissive moisture sensor. (A) iFFP fibre array resistance plot showing the linear response of resistance as a function of relative humidity. (B) Commercial humidity sensor *versus* iFFP PEDOT:PSS sensor signal in response to a moisture pulse. (C) Schematic of the multiple-stage sensor with three tiers (L_1 to L_3), with the corresponding time-resolved resistance measurement in (D) and processed images of mist rising up from L_1 to L_3 in (E).

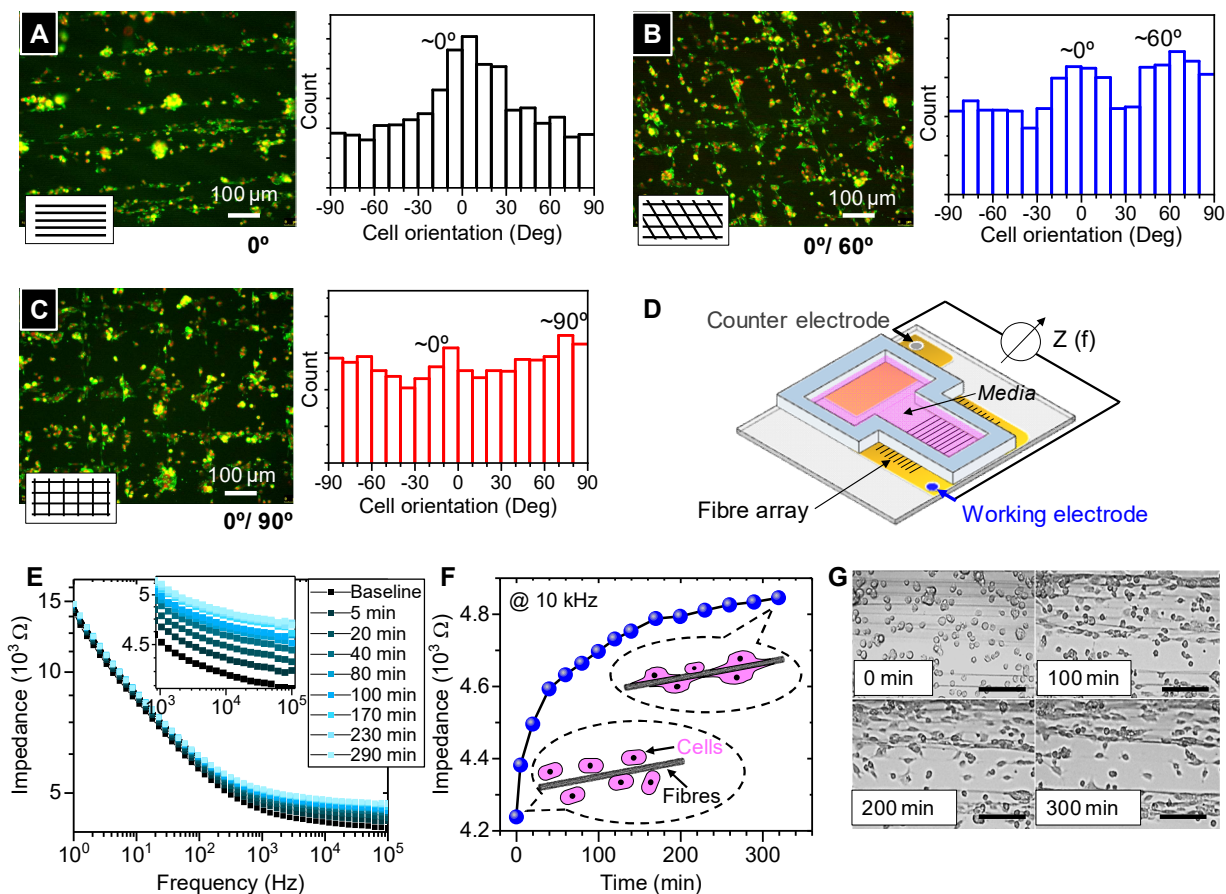


Fig. 4. PEDOT:PSS fibres bio-impedimetric sensor. (A, B and C) fluorescence images (red=nucleus, green=F-actin) showing fibre array guiding cellular orientation, as confirmed by the orientation histograms. (D) Schematic of the impedimetric sensor. (E) time-lapsed *in-situ* impedance measurement as a function of frequency. (F) Plot of impedance at 10kHz *versus* time (after cell sedimentation), to compare with the time-lapsed imaging of cell-fibre interaction in (G). Scale bar = 150 μm .

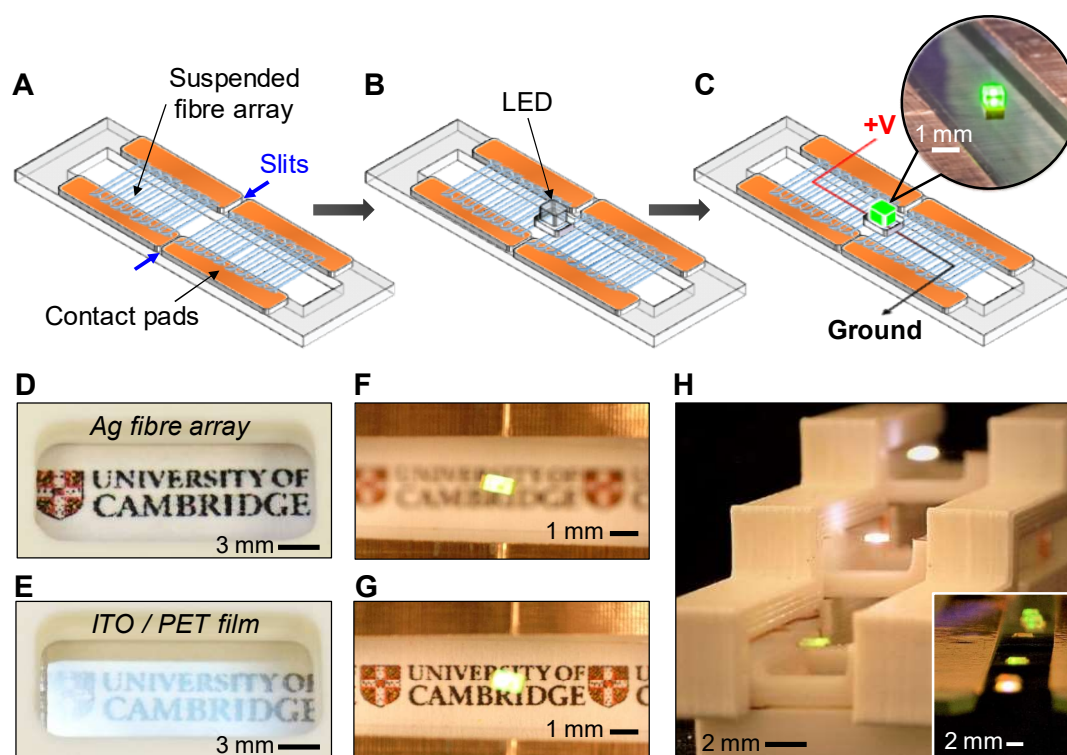


Fig. 5. Architecture of 3D-layered 'floating circuit'. (A, B and C) Schematics showing the successive steps to connect a LED on the suspended transparent Ag fibre array. (D-E) Photos showing oblique light response from a suspended fibre array *versus* standard ITO/PET film. (F-G) Top views of the 'floating circuit', in- and out- of focus of the LED light. (H) Creating a 3D-layered circuit architecture by combining 3D printing, insert showing multiple LEDs connection on a single array of PEDOT:PSS fibres.

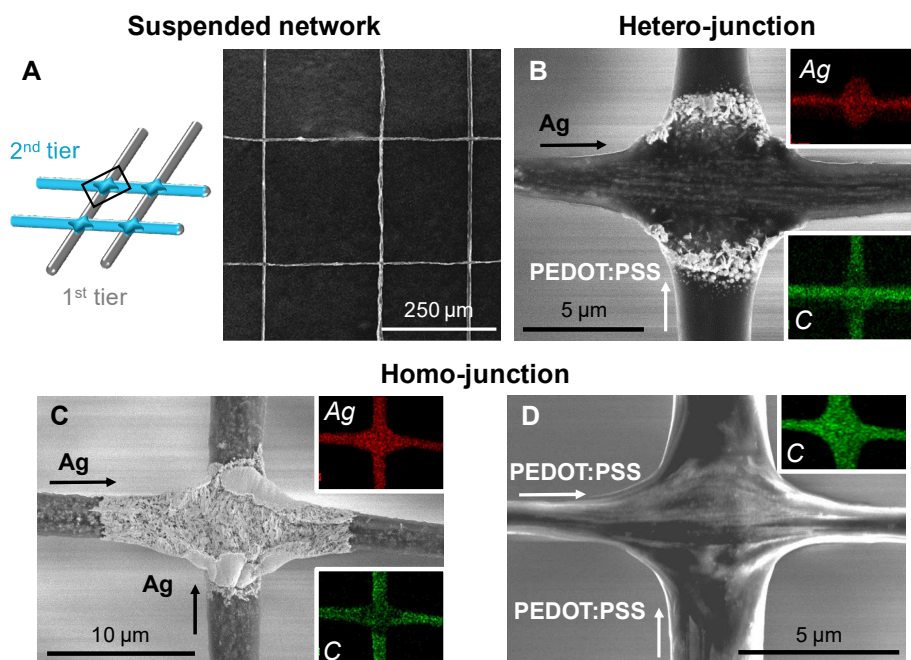


Fig. 6. Architecture of suspended cross-junctioned fibres. (A) Schematic and an SEM global view of suspended Ag and PEDOT:PSS junctioned fibre network. (B) Magnification of a single junction of (A) and EDX profiles showing Silver (Ag) and Carbon (C) distribution at the junction. (C-D) SEM images showing homo-junctions of Ag or PEDOT:PSS fibres with the associated EDX mapping, respectively.

Supplementary Materials

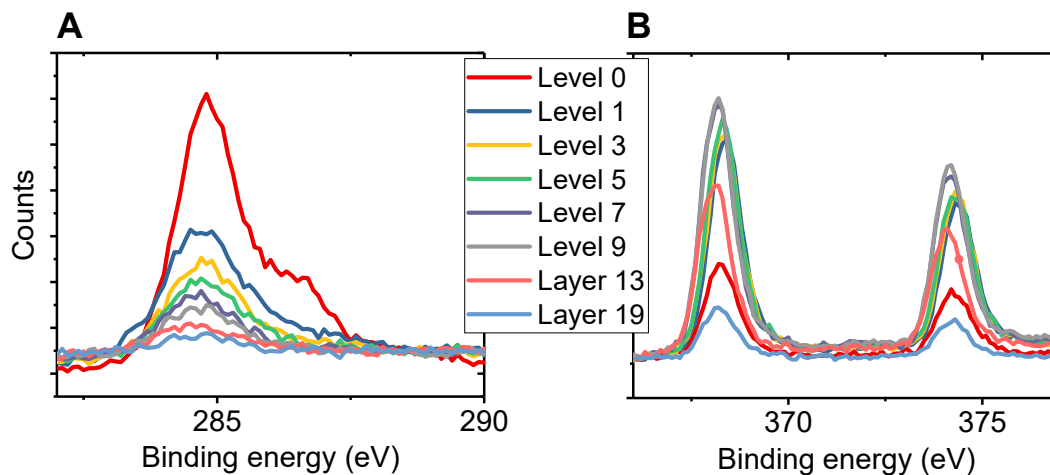


Fig. S1. XPS high-resolution results of depth profiling on fibre bond area. (A) Carbon 1s peak values on different etching layers, the main peak at 284.7 eV corresponds to C 1s (C-C) binding energy **(B)** Silver 3d peak values on different etching layers, main peaks at 368.3 and 374.3 eV correspond to Ag 3d_{5/2} and Ag 3d_{5/3} binding energies (19).

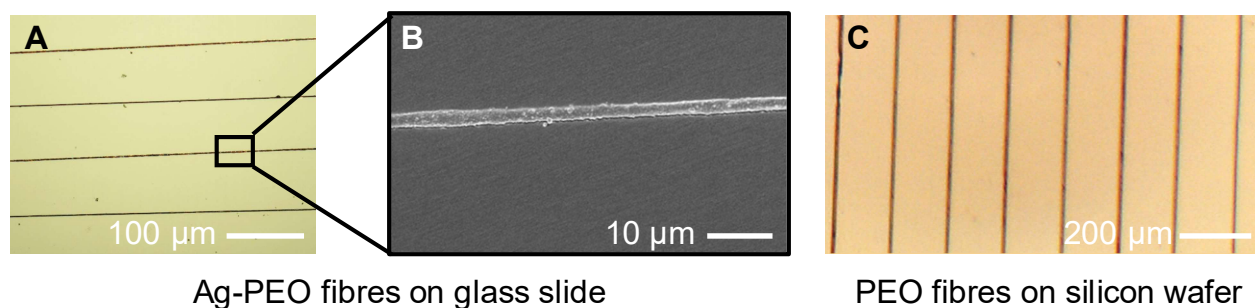


Fig. S2. Versatility of iFFP technique in depositing fibres onto various substrates. By applying a low electrical field between the needle and the substrate ($\sim 400 \text{ V.cm}^{-1}$), iFFP could deposit fibres onto various substrates. As shown, Ag fibres are printed onto glass slide (**A-B**), and the conductivity is consistent with suspended Ag fibre array. iFFP could also deposit PEO fibres onto silicon conducting substrate as shown in (**C**).

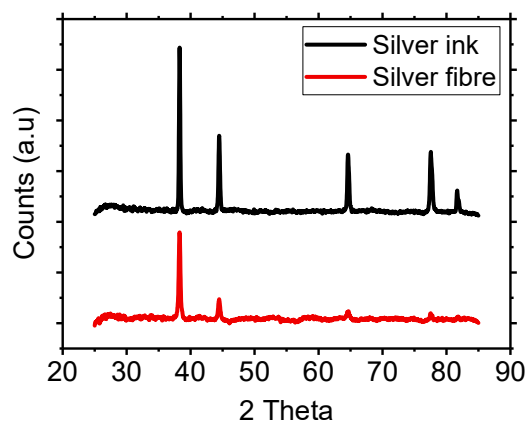


Fig. S3. XRD on heated silver precursor droplet and Ag fibre. Main peaks of 2θ values at 38.1, 44.3, 64.5, and 77.4, corresponding to the (111), (200), (220) and (311) crystal faces of the face center cubic of crystalline silver (*fcc*), are observed on both heated silver precursor droplet and Ag fibres.

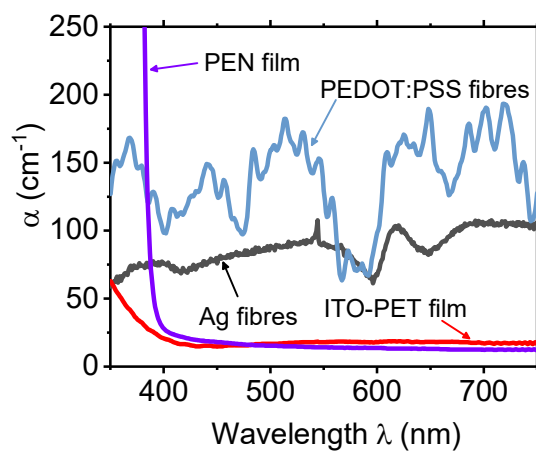


Fig. S4. Absorbance of Ag, PEDOT:PSS fibres, PEN and ITO-PET films in the 350-750 nm region. The absorption coefficient $\alpha = \ln(10)A/d$, where A is the absorbance and d the thickness of the sample.

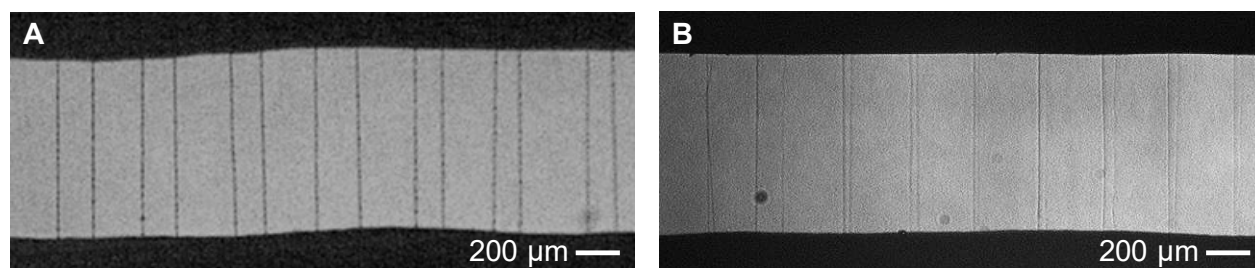


Fig. S5. PEDOT:PSS fibres stability post-liquid immersion. Suspended PEDOT:PSS fibre array retains their designated patterns and orientation before **(A)** and after **(B)** immersed in cell culture media for 3 days.

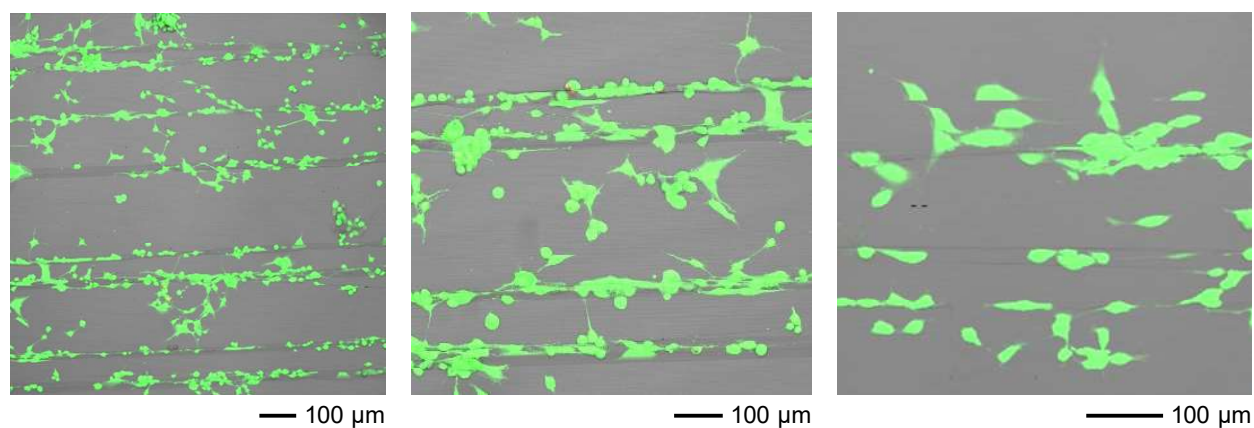


Fig. S6. Cell viability assay on PEDOT:PSS fibres. Human glioblastoma cells (U-87a) were seeded onto PEDOT:PSS fibre arrays on glass cover slides, and live dead assay (Invitrogen) was performed following manufacturer's protocol on day 3, as shown in the images above. It is shown that all the cells are viability as only green fluorescent (live) cells were observed, with no red fluorescent (dead) cells. From left to right : zooming.

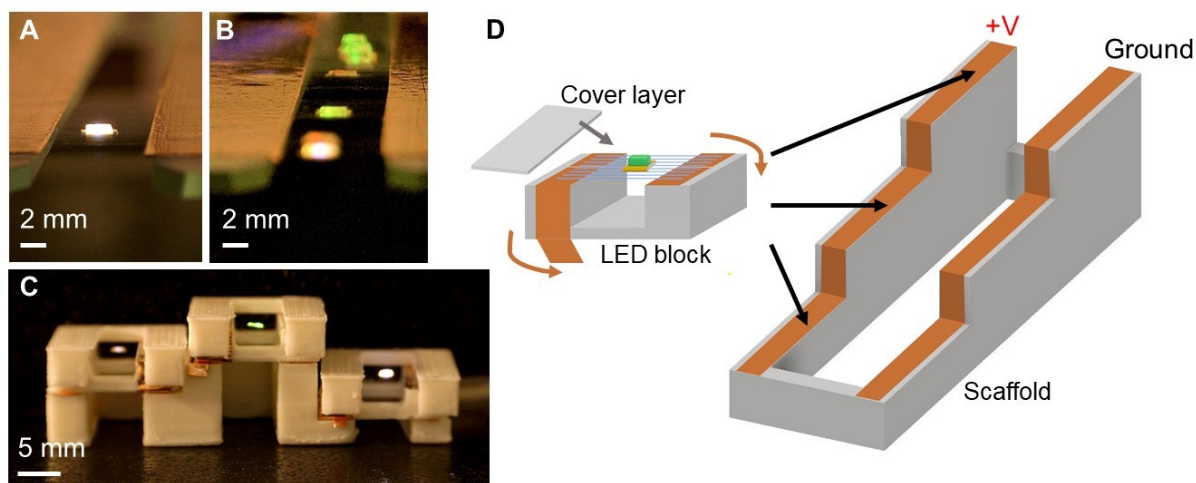


Fig. S7. 3D fibre based circuit configuration and LED lights placed on top of PEDOT:PSS fibre arrays. (A) A single white LED light is placed on top of PEDOT:PSS fibre array. **(B)** Multiple LED lights placed on top of PEDOT:PSS fibre array. **(C)** Another configuration of 3D circuit fabricated with 3D printed plastics and Ag fibre array. **(D)** Schematic showing the assembly of 3D circuit showing in **Fig.5 H**. Copper tapes are used to cover the surface and also bottom of the 3D printed block, and then LED light is placed on top of the fibre array, a protective cover layer is placed on top. This LED block can be placed onto scaffolds with different designs.